npj | quantum materials

Article

Published in partnership with Nanjing University

https://doi.org/10.1038/s41535-024-00635-5

Two-dimensional phase diagram of the charge density wave in doped CsV_3Sb_5

Linwei Huai[1,5], Hongyu Li[1,5], Yulei Han[2,5], Yang Luo[1,5], Shuting Peng[1], Zhiyuan Wei[1], Jianchang Shen[1], Bingqian Wang[1], Yu Miao[1], Xiupeng Sun[1,3], Zhipeng Ou[1], Bo Liu[1], Xiaoxiao Yu[1], Ziji Xiang[1], Min-Quan Kuang[4], Zhenhua Qiao[1] ✉, Xianhui Chen[1] ✉ & Junfeng He[1] ✉

Kagome superconductors AV_3Sb_5 (A = K, Rb and Cs) have attracted much recent attention due to the coexistence of multiple exotic orders. Among them, the charge density wave (CDW) order has been shown to host various unconventional behaviors. Here, we investigate the CDW order by a combination of both bulk and surface doping methods. While element substitutions in bulk doping change both carriers and the crystal lattice, the surface doping primarily tunes the carrier concentration. As such, our results reveal a two-dimensional phase diagram of the CDW in doped CsV_3Sb_5. In the lightly bulk doped regime, the existence of CDW order is reversible by tuning the carrier concentration. But excessive bulk doping permanently destroys the CDW, regardless of the carrier doping level. These results provide insights to the origin of the CDW from both electronic and structural degrees of freedom. They also open an avenue for manipulating the exotic CDW order in Kagome superconductors.

Kagome metals have attracted much attention due to the special lattice structure and associated physical properties[1–4]. The ongoing interest is further energized by Kagome superconductors AV_3Sb_5 (A = K, Rb and Cs), in which many exotic phenomena have been observed[5–50], ranging from superconductivity[5–9], charge density wave (CDW)[5,6,10–19], nematic order[20,21], pair density wave[22], topological states[5,23,24] and the time-reversal symmetry breaking state[17,25–27]. While the origins of these phenomena remain unclear, it is interesting that most of them are closely related to the CDW state[5,6,10–19]. In this regard, it is important to understand the driving mechanism of the CDW. Two scenarios have been primarily suggested[15,29–36]. The first is associated with the electronic instability, presumably driven by Fermi surface nesting[15,29–32], and the second is related to the structural instability via electron-phonon coupling[15,32–36]. In order to examine the origin, doping evolution of the CDW has been experimentally investigated by chemical element substitutions[38–45]. Nevertheless, both the carrier concentration and the crystal lattice have been changed in this process. Surface doping has also been performed by Cs surface deposition[46]. Comparing to the bulk element substitutions, the surface doping primarily induces carriers (electrons) to the surface layers of the samples[46]. Its application on a pristine CsV_3Sb_5 compound has led to a monotonic suppression of the CDW order[46]. Despite the continuous efforts, it remains challenging to differentiate the roles played by electron and lattice degrees of freedom[38–46].

In this paper, we investigate the evolution of CDW order in CsV_3Sb_5 via a combination of both bulk and surface doping. Angle-resolved photoemission spectroscopy (ARPES) measurements, which are sensitive to both doping methods[51], have been carried out to track the evolution of the CDW order in this material. First, Ti substitution of V is applied to the bulk crystal of CsV_3Sb_5, which induces hole doping and modifies the V Kagome net simultaneously. Continuous Cs surface deposition is then carried out on the $CsV_{3-x}Ti_xSb_5$ samples, which gradually induces electrons to compensate the holes doped by the Ti substitution. It is interesting that the CDW order is reversible as a function of carrier concentration in the lightly Ti doped regime. This is evidenced by the CDW gap, which disappears with Ti doping, but reappears with Cs surface deposition. However, excessive Ti bulk doping permanently destroys the CDW order, which becomes irreversible by tuning the carrier concentration. These results reveal a two-dimensional phase diagram of the CDW order in doped CsV_3Sb_5, and provide key insights to the associated driving mechanism.

[1]Department of Physics and CAS Key Laboratory of Strongly-coupled Quantum Matter Physics, University of Science and Technology of China, Hefei, Anhui 230026, China. [2]Department of Physics, Fuzhou University, Fuzhou, Fujian 350108, China. [3]Hefei National Laboratory, University of Science and Technology of China, Hefei 230088, China. [4]Chongqing Key Laboratory of Micro & Nano Structure Optoelectronics, and School of Physical Science and Technology, Southwest University, Chongqing 400715, China. [5]These authors contributed equally: Linwei Huai, Hongyu Li, Yulei Han, Yang Luo. ✉e-mail: qiao@ustc.edu.cn; chenxh@ustc.edu.cn; jfhe@ustc.edu.cn

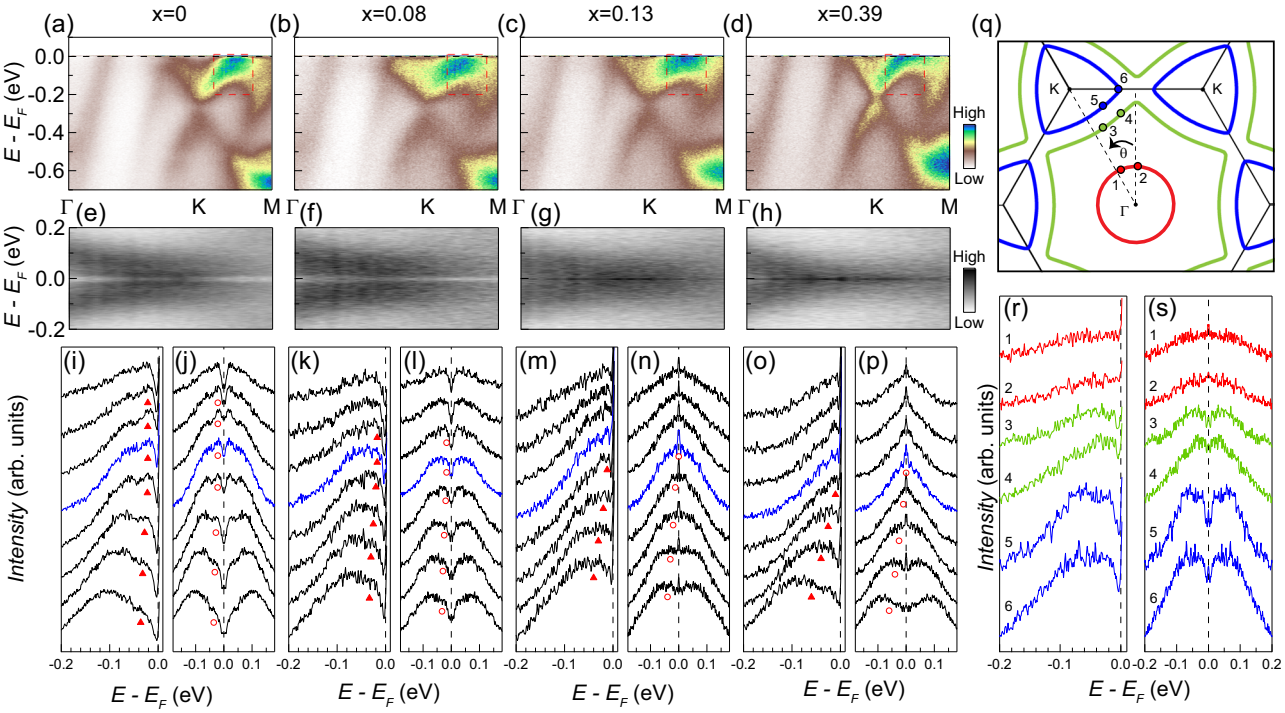

Fig. 1 | Electronic structure of $CsV_{3-x}Ti_xSb_5$ as a function of the Ti substitution level, measured at 10 K. a–d Photoelectron intensity plot of the band structure along the Γ-*K*-*M* direction on $CsV_{3-x}Ti_xSb_5$ samples with $x = 0$ (**a**), 0.08 (**b**), 0.13 (**c**) and 0.39 (**d**). **e–h** symmetrized low energy spectrum near the vHs region in (**a–d**). **i–p** EDCs in the red dotted boxes in (**a–d**). The EDCs are divided by the Fermi–Dirac function (**i**, **k**, **m**, **o**) and symmetrized with respect to E_F (**j**, **l**, **n**, **p**), respectively. EDCs at the Fermi momenta are highlighted in blue. The EDC peaks are marked by triangles and circles. **q** Schematic Fermi Surface of $CsV_{3-x}Ti_xSb_5$ ($x = 0.03$). **r**, **s** EDCs at representative momentum points. The momentum locations of the points are shown in (**q**).

Results

Evolution of CDW as a function of bulk and surface doping

Figure 1 shows the electronic structure of $CsV_{3-x}Ti_xSb_5$ as a function of Ti bulk doping (see Supplementary Note 1 and Supplementary Fig. 1 for the sample characterization), measured at a low temperature (10 K). The photoemission measurements are carried out along Γ-*K*-*M* direction, where the CDW gap is most clearly revealed in the pristine CsV_3Sb_5 compound[32,47,48]. In order to visualize the evolution of the gap, low energy spectra around the van Hove singularity (vHs, marked by the red dotted boxes in Fig. 1a–d) are symmetrized with respect to the Fermi level (E_F) (Fig. 1e–h). It is clear that the CDW gap decreases with Ti doping and disappears at doping levels $x \geq 0.13$ (Fig. 1g, h). This is quantified by the corresponding energy distribution curves (EDCs) (Fig. 1i–p), where both Fermi–Dirac divided and symmetrized EDCs reveal the same doping evolution. Momentum dependence of the CDW gap is also examined on a Ti doped sample ($x = 0.03$), which is largely consistent with that of the pristine CsV_3Sb_5 compound, but with an overall smaller magnitude of the gap (Fig. 1q–s).

Next, Cs surface doping is gradually carried out on the $CsV_{3-x}Ti_xSb_5$ ($x = 0.13$) sample at a fixed low temperature (10 K). As illustrated in Fig. 1 (also shown in Fig. 2a, e, f), the CDW gap is completely suppressed by Ti doping in this sample. Upon Cs surface doping, a slight downward shift of the V bands is observed (Fig. 2a–d, for example, see the band top near *K* point, marked by the black triangles). Most strikingly, a spectral weight suppression starts to appear near E_F, indicating the possible reappearance of an energy gap. This behavior is quantitatively revealed by the EDCs around the vHs region, where an energy gap gradually forms at E_F as a function of the Cs surface doping (Fig. 2e–l). In order to examine whether the gap opening is associated with the reappearance of the CDW order or created by extrinsic effects (e.g., a possible localization effect induced by disorders), the Cs surface doping is repeated on the $CsV_{3-x}Ti_xSb_5$ ($x = 0.13$) sample, but at a much higher temperature (100 K). Different from the behavior at low temperature, now the system remains gapless after the Cs surface doping (Fig. 2m–r). Nevertheless, the energy gap starts to appear on the band near the vHs (with V d-orbitals) when the temperature is cooled down to ~40 K (Fig. 2o, p). This gap becomes more evident at a lower temperature of 10 K (Fig. 2o, p). On the contrary, the band around the Γ point (with the Sb P-orbital) remains gapless at all temperatures (Fig. 2q, r). The above temperature and momentum (orbital) dependent behaviors of the gap are highly consistent with those of the CDW gap, demonstrating the reappearance of the CDW order in this system.

In order to further understand the evolution of the CDW order, the surface Cs doping is carried out on another $CsV_{3-x}Ti_xSb_5$ sample, but with a higher bulk doping level ($x = 0.39$) at 10 K. Apparently, the CDW order is completely suppressed in this sample before the Cs surface doping, evidenced by the absence of the CDW gap (Fig. 3a, e, i, j). Upon the Cs doping, an overall downward shift of the V bands is observed as before (Fig. 3a–d). We note that excessive Cs doping has been applied on this sample (Fig. 3c, d) to ensure that the holes induced by the higher level of Ti substitution are sufficiently compensated and a similar total carrier concentration is achieved as before. This is evidenced by similar positions of the energy features on the band structure of the two samples after Cs deposition (e.g., compare the band top between *Γ* and *K* in Figs. 2c, d, n and 3c, d, marked by the black triangles). However, distinct from the earlier case, no evidence of gap opening is observed on the $CsV_{3-x}Ti_xSb_5$ ($x = 0.39$) sample with Cs surface doping. This gapless state remains robust, regardless of the electron doping level induced by the Cs surface deposition (Fig. 3e–p).

Two-dimensional phase diagram of the CDW order

The above bulk and surface doping dependent measurements (Fig. 4a–c) reveal a two-dimensional phase diagram of the CDW in doped CsV_3Sb_5 (Fig. 4d). First, the CDW order is monotonically suppressed as a function of the Ti bulk doping, and the CDW gap

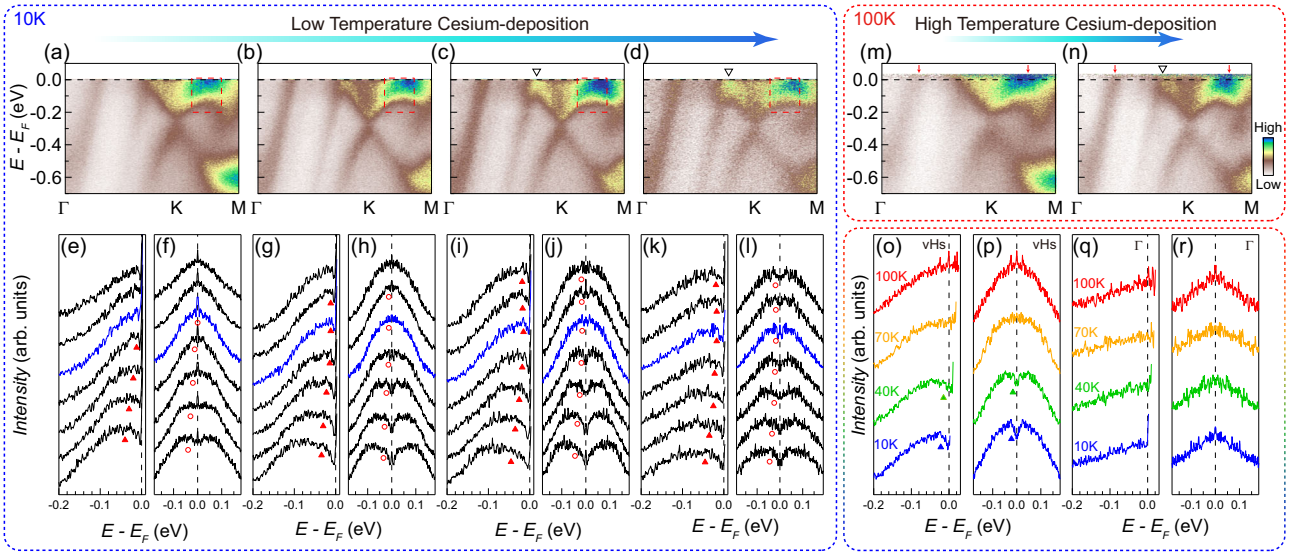

Fig. 2 | Evolution of the electronic structure with Cs surface doping on the $CsV_{3-x}Ti_xSb_5$ (x = 0.13) sample. a–d Photoelectron intensity plot of the band structure along the Γ-*K*-*M* direction as a function of Cs surface doping at 10 K. **e–l** EDCs in the red dotted boxes in (**a–d**). The EDCs are divided by the Fermi–Dirac function (**e**, **g**, **i**, **k**) and symmetrized with respect to E_F (**f**, **h**, **j**, **l**), respectively. EDCs at the Fermi momenta are highlighted in blue. **m**, **n** Photoelectron intensity plot of the band structure along the Γ-*K*-*M* direction before (**m**) and after (**n**) Cs surface deposition at 100 K. The red arrows mark the Fermi momenta. **o**, **p** Temperature dependence of the EDC at the Fermi momentum near the vHs. To reveal the gap opening, the EDC is divided by the Fermi–Dirac function (**o**) and symmetrized with respect to E_F (**p**), respectively. **q**, **r** Same as (**o**, **p**), but measured at the Fermi momentum near Γ. The black triangles in (**c**, **d**, **n**) mark the band top between Γ and *K*.

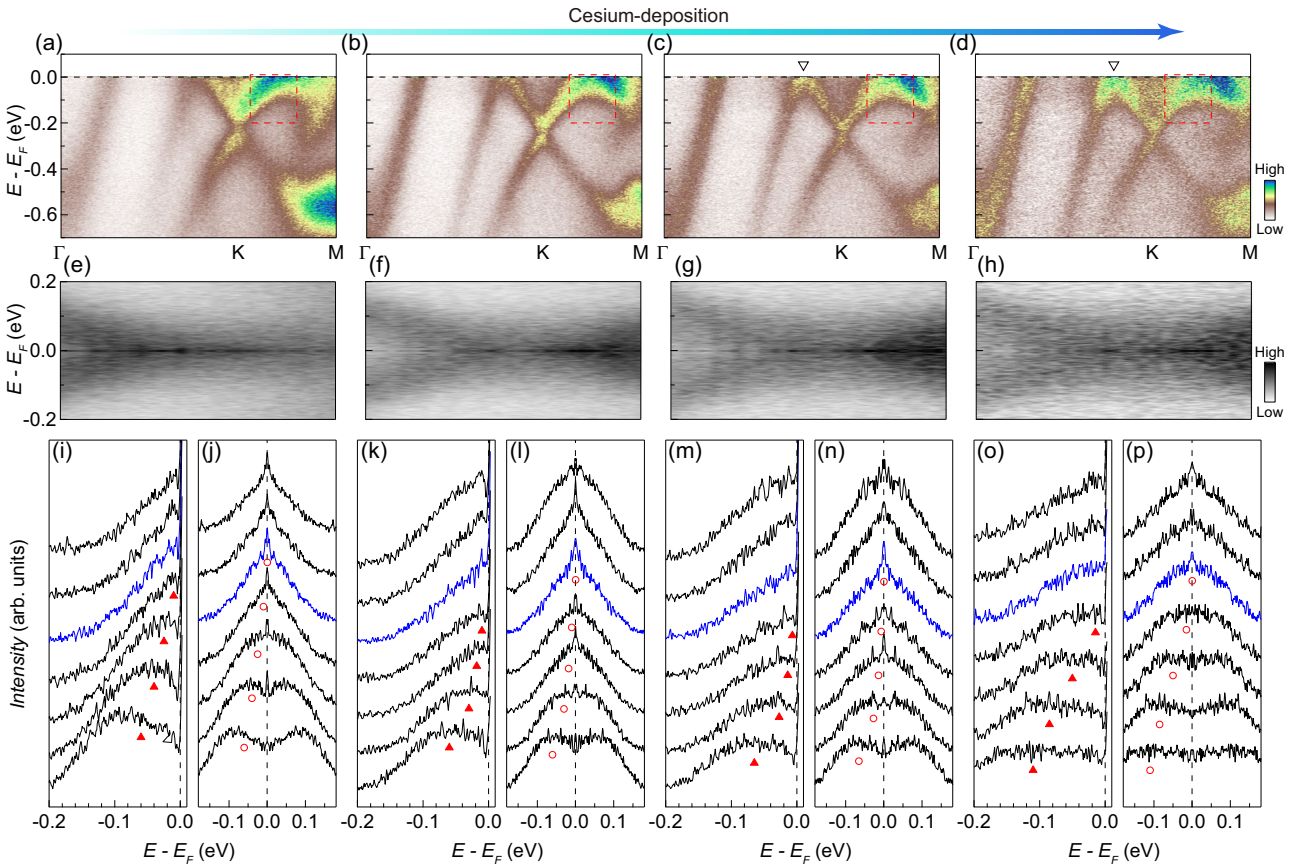

Fig. 3 | Evolution of the electronic structure with Cs surface doping on the $CsV_{3-x}Ti_xSb_5$ (x = 0.39) sample. a–d Photoelectron intensity plot of the band structure along the Γ-*K*-*M* direction as a function of Cs surface doping at 10 K. The black triangles in (**c**, **d**) mark the band top between Γ and *K*. **e–h** Symmetrized low energy spectrum near the vHs region in (**a–d**). **i–p** EDCs in the red dotted boxes in (**a–d**). The EDCs are divided by the Fermi–Dirac function (**i**, **k**, **m**, **o**) and symmetrized with respect to E_F (**j**, **l**, **n**, **p**), respectively. EDCs at the Fermi momenta are highlighted in blue.

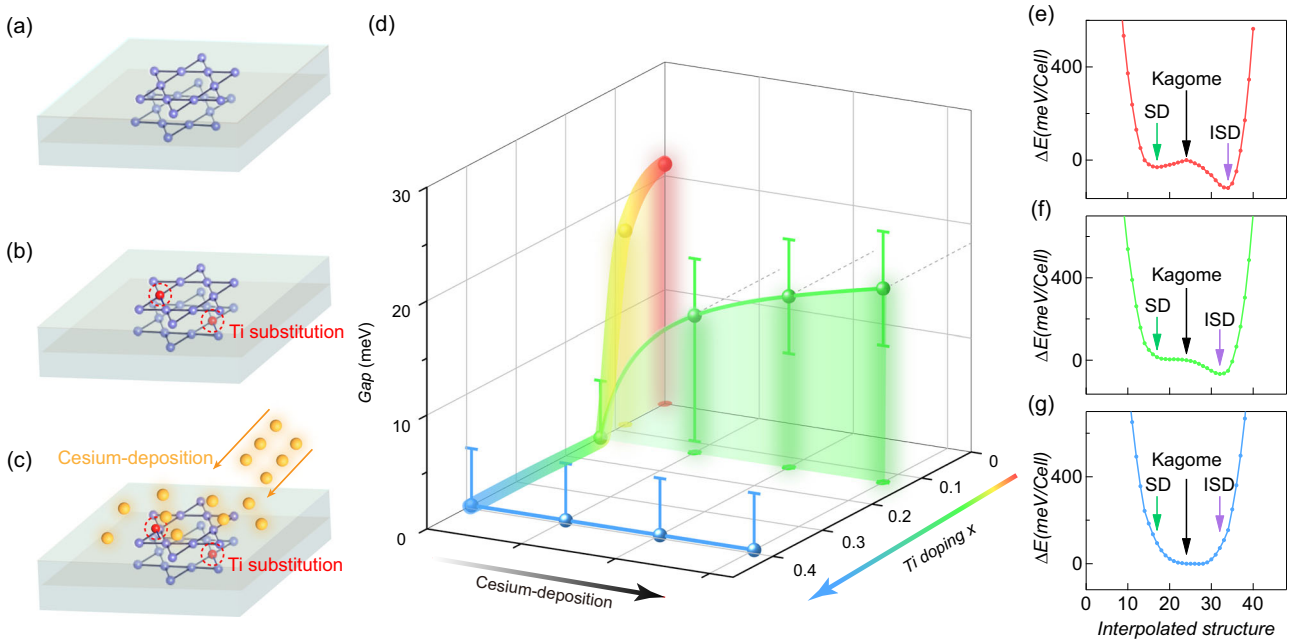

Fig. 4 | Two-dimensional phase diagram of the CDW in doped CsV_3Sb_5 and total energy profiles of $CsV_{3-x}Ti_xSb_5$. a–c Schematics of the doping processes. d two-dimensional phase diagram of the CDW gap in CsV_3Sb_5 as a function of Ti substitution and Cs surface deposition. **e–g** Calculated total energy of pristine CsV_3Sb_5 (**e**), $CsV_{3-x}Ti_xSb_5$ ($x = 0.125$) (**f**), and $CsV_{3-x}Ti_xSb_5$ ($x = 0.375$) (**g**). ΔE represents the relative total energy with respect to that of the Kagome structure. It is shown in the $2 \times 2 \times 2$ supercell (72 atoms) for all cases.

disappears at the doping level of $x = 0.13$. Then, continuous surface doping at the fixed Ti doping level ($x = 0.13$) leads to the reappearance of the CDW gap. However, the Cs surface doping shows little effect on the sample with a higher Ti doping level of $x = 0.39$. The sample remains gapless, regardless of the surface doping level.

Discussion

Finally, we discuss the implications of such an experimental phase diagram. First, the Ti bulk doping changes both the carrier concentration and the lattice of the material. On one hand, the substitution of V atoms by Ti atoms effectively induces holes into the Kagome layer. On the other hand, the new Ti atoms would inevitably modify the original V Kagome net and affect the lattice vibration. The totality of these effects results in the suppression of the CDW order. Second, the Cs surface doping primarily induces electrons to the sample. In pristine CsV_3Sb_5, a suppression of CDW with Cs surface doping has been reported[46], where the surface induced electrons may shift the carrier concentration away from the optimal doping. On the other hand, the electrons induced by Cs surface deposition would compensate the holes doped by Ti substitution in the $CsV_{3-x}Ti_xSb_5$ compound. The reappearance of the CDW order in the lightly Ti doped regime ($x = 0.13$) demonstrates that the carrier concentration is important for the CDW. It also provides a tuning knob to manipulate the CDW order. However, the suppression of CDW order becomes irreversible by surface doping in the heavily bulk doped regime ($x = 0.39$), which indicates that the carrier concentration is not the only controlling parameter of the CDW. In order to better understand the role of lattice, we have calculated the total energy profiles of $CsV_{3-x}Ti_xSb_5$[15,52,53] at the Ti doping levels of $x = 0$ (pristine CsV_3Sb_5, Fig. 4e), $x = 0.125$ (Fig. 4f) and $x = 0.375$ (Fig. 4g) (see Supplementary Note 2 for the details of the calculation), which are very close to the doping levels of the samples measured in the experiments. It is clear that the Kagome structure is unstable in the pristine compound, in which the Inverse Star of David (ISD) structure has the lowest total energy[15] (see Supplementary Fig. 2 for the schematics of Kagome, Star of David and Inverse Star of David structures). This lattice instability persists to the Ti doping level of $x = 0.125$ (Fig. 4f), but disappears at $x = 0.375$ (Fig. 4g). These results, when combined with the experimental observations, point to a unified understanding of the two-dimensional phase diagram. The coexistence of lattice instability and appropriate amount of carrier concentration is needed to establish the CDW order in the CsV_3Sb_5 system. In this regard, the lattice instability naturally provides a tendency towards the CDW transition, and the carrier concentration serves as a tuning knob to change the magnitude (and possibly correlation length) of the CDW order. When the lattice instability persists (for example, in a finite Ti doping range around $x = 0.13$), the CDW order is reversible by tuning the carrier concentration. In addition, the change of carrier concentration may also affect the electronic correlation in the material system (for example, via screening effect). In this sense, our observations can also reconcile the earlier reports that multiple unconventional properties in the CDW state are associated with electronic correlation[20,22,25–27], but the electronic instability itself is insufficient to drive the CDW phase transition[34,35,49,54].

In summary, by utilizing high-resolution ARPES measurements, we have revealed a two-dimensional phase diagram of the CDW in CsV_3Sb_5 as a function of both Ti bulk substitution and Cs surface deposition. The distinct evolutions in this phase diagram reveal the roles played by both electrons and lattice. These observations provide key insights to understand the driving mechanism of the CDW order in Kagome metals.

Methods

Sample growth

Single crystals of $CsV_{3-x}Ti_xSb_5$ were grown by self-flux growth method. The details of the crystal growth and characterizations are described in the Supplementary Note 1.

ARPES measurements

The samples were cleaved in situ with a base pressure of better than 5×10^{-11} Torr. ARPES measurements were carried out at our lab-based ARPES system using 21.2 eV photons with a total energy resolution of ~3 meV. The Fermi level was obtained by measuring the polycrystalline Au in electrical contact with the samples.

Data availability

All data generated or analyzed in this study are included in this article and the Supplementary Information.

Received: 19 September 2023; Accepted: 26 February 2024;
Published online: 09 March 2024

References

1. Helton, J. S. et al. Spin dynamics of the spin-1/2 kagome lattice antiferromagnet $ZnCu_3(OH)_6Cl_2$. *Phys. Rev. Lett.* **98**, 107204 (2007).
2. Guo, H. M. & Franz, M. Topological insulator on the kagome lattice. *Phys. Rev. B* **80**, 113102 (2009).
3. Liu, E. et al. Giant anomalous Hall effect in a ferromagnetic kagome-lattice semimetal. *Nat. Phys.* **14**, 1125–1131 (2018).
4. Kang, M. et al. Topological flat bands in frustrated kagome lattice CoSn. *Nat. Commun.* **11**, 4004 (2020).
5. Ortiz, B. R. et al. CsV_3Sb_5: A Z_2 topological kagome metal with a superconducting ground state. *Phys. Rev. Lett.* **125**, 247002 (2020).
6. Ortiz, B. R. et al. Superconductivity in the Z_2 kagome metal KV_3Sb_5. *Phys. Rev. Mater.* **5**, 034801 (2021).
7. Yin, Q. et al. Superconductivity and normal-state properties of kagome metal RbV_3Sb_5 single crystals. *Chin. Phys. Lett.* **38**, 037403 (2021).
8. Ni, S. et al. Anisotropic superconducting properties of kagome metal CsV_3Sb_5. *Chin. Phys. Lett.* **38**, 057403 (2021).
9. Chen, K. Y. et al. Double superconducting dome and triple enhancement of Tc in the kagome superconductor CsV_3Sb_5 under high pressure. *Phys. Rev. Lett.* **126**, 247001 (2021).
10. Zhao, H. et al. Cascade of correlated electron states in the kagome superconductor CsV_3Sb_5. *Nature* **599**, 216–221 (2021).
11. Liang, Z. et al. Three-dimensional charge density wave and surface-dependent vortex-core states in a kagome superconductor CsV_3Sb_5. *Phys. Rev. X* **11,**031026 (2021).
12. Ortiz, B. R. et al. Fermi surface mapping and the nature of charge-density-wave order in the kagome superconductor CsV_3Sb_5. *Phys. Rev. X* **11**, 041030 (2021).
13. Li, H. et al. Observation of unconventional charge density wave without acoustic phonon anomaly in kagome superconductors AV_3Sb_5 (A= Rb, Cs). *Phys. Rev. X* **11**, 031050 (2021).
14. Yu, F. H. et al. Unusual competition of superconductivity and charge-density-wave state in a compressed topological kagome metal. *Nat. Commun.* **12**, 3645 (2021).
15. Tan, H. et al. Charge density waves and electronic properties of superconducting kagome metals. *Phys. Rev. Lett.* **127**, 046401 (2021).
16. Liu, Z. et al. Charge-density-wave-induced bands renormalization and energy gaps in a kagome superconductor RbV_3Sb_5. *Phys. Rev. X* **11**, 041010 (2021).
17. Jiang, Y. X. et al. Unconventional chiral charge order in kagome superconductor KV_3Sb_5. *Nat. Mater.* **20**, 1353–1357 (2021).
18. Song, B. et al. Anomalous enhancement of charge density wave in kagome superconductor CsV_3Sb_5 approaching the 2D limit. *Nat. Commun.* **14**, 2492 (2023).
19. Song, Y. et al. Competition of superconductivity and charge density wave in selective oxidized CsV_3Sb_5 thin flakes. *Phys. Rev. Lett.* **127**, 237001 (2021).
20. Nie, L. et al. Charge-density-wave-driven electronic nematicity in a kagome superconductor. *Nature* **604**, 59–64 (2022).
21. Xiang, Y. et al. Twofold symmetry of c-axis resistivity in topological kagome superconductor CsV_3Sb_5 with in-plane rotating magnetic field. *Nat. Commun.* **12**, 6727 (2021).
22. Chen, H. et al. Roton pair density wave in a strong-coupling kagome superconductor. *Nature* **599**, 222–228 (2021).
23. Hu, Y. et al. Topological surface states and flat bands in the kagome superconductor CsV_3Sb_5. *Sci. Bull.* **67**, 495–500 (2022).
24. Fu, Y. et al. Quantum transport evidence of topological band structures of kagome superconductor CsV_3Sb_5. *Phys. Rev. Lett.* **127**, 207002 (2021).
25. Mielke, C. III et al. Time-reversal symmetry-breaking charge order in a kagome superconductor. *Nature* **602**, 245–250 (2022).
26. Yu, L. et al. Evidence of a hidden flux phase in the topological kagome metal CsV_3Sb_5. Preprint at https://arxiv.org/abs/2107.10714 (2021).
27. Khasanov, R. et al. Time-reversal symmetry broken by charge order in CsV_3Sb_5. *Phys. Rev. Res.* **4**, 023244 (2022).
28. Guguchia, Z., Khasanov, R. & Luetkens, H. Unconventional charge order and superconductivity in kagome-lattice systems as seen by muon-spin rotation. *npj Quantum Mater.* **8**, 41 (2023).
29. Cho, S. et al. Emergence of new van Hove singularities in the charge density wave state of a topological kagome metal RbV_3Sb_5. *Phys. Rev. Lett.* **127**, 236401 (2021).
30. Lou, R. et al. Charge-density-wave-induced peak-dip-hump structure and the multiband superconductivity in a kagome superconductor CsV_3Sb_5. *Phys. Rev. Lett.* **128**, 036402 (2022).
31. Zhou, X. et al. Origin of charge density wave in the kagome metal CsV_3Sb_5 as revealed by optical spectroscopy. *Phys. Rev. B* **104**, L041101 (2021).
32. Luo, H. et al. Electronic nature of charge density wave and electron-phonon coupling in kagome superconductor KV_3Sb_5. *Nat. Commun.* **13**, 273 (2022).
33. Uykur, E. et al. Optical detection of the density-wave instability in the kagome metal KV_3Sb_5. *npj Quantum Mater.* **7**, 16 (2022).
34. Xie, Y. et al. Electron-phonon coupling in the charge density wave state of CsV_3Sb_5. *Phys. Rev. B* **105**, L140501 (2022).
35. Ye, Z. et al. Structural instability and charge modulations in the kagome superconductor AV_3Sb_5. *Phys. Rev. B* **105**, 245121 (2022).
36. Wenzel, M. et al. Optical study of RbV_3Sb_5: multiple density-wave gaps and phonon anomalies. *Phys. Rev. B* **105**, 245123 (2022).
37. Wenzel, M. et al. Pressure evolution of electron dynamics in the superconducting kagome metal CsV_3Sb_5. *npj Quantum Mater.* **8**, 45 (2023).
38. Oey, Y. M. et al. Fermi level tuning and double-dome superconductivity in the kagome metal $CsV_3Sb_{5-x}Sn_x$. *Phys. Rev. Mater.* **6**, L041801 (2022).
39. Li, J. et al. Strong-coupling superconductivity and weak vortex pinning in Ta-doped CsV_3Sb_5 single crystals. *Phys. Rev. B* **106**, 214529 (2022).
40. Li, Y. et al. Tuning the competition between superconductivity and charge order in the kagome superconductor $Cs(V_{1-x}Nb_x)_3Sb_5$. *Phys. Rev. B* **105**, L180507 (2022).
41. Ding, G., Wo, H., Gu, Y., Gu, Y. & Zhao, J. Effect of chromium doping on superconductivity and charge density wave order in the kagome metal $Cs(V_{1-x}Cr_x)_3Sb_5$. *Phys. Rev. B* **106**, 235151 (2022).
42. Liu, M. et al. Evolution of superconductivity and charge density wave through Ta and Mo doping in CsV_3Sb_5. *Phys. Rev. B* **106**, L140501 (2022).
43. Liu, Y. et al. Enhancement of superconductivity and suppression of charge-density wave in As-doped CsV_3Sb_5. *Phys. Rev. Mater.* **6**, 124803 (2022).
44. Yang, H. et al. Titanium doped kagome superconductor $CsV_{3-x}Ti_xSb_5$ and two distinct phases. *Sci. Bull.* **67**, 2176–2185 (2022).
45. Hou, J. et al. Effect of hydrostatic pressure on the unconventional charge density wave and superconducting properties in two distinct phases of doped kagome superconductors $CsV_{3-x}Ti_xSb_5$. *Phys. Rev. B* **107**, 144502 (2023).
46. Nakayama, K. et al. Carrier injection and manipulation of charge-density wave in kagome superconductor CsV_3Sb_5. *Phys. Rev. X* **12**, 011001 (2022).
47. Nakayama, K. et al. Multiple energy scales and anisotropic energy gap in the charge-density-wave phase of the kagome superconductor CsV_3Sb_5. *Phys. Rev. B* **104**, L161112 (2021).
48. Wang, Z. et al. Distinctive momentum dependent charge-density-wave gap observed in CsV_3Sb_5 superconductor with topological

Kagome lattice. Preprint at https://arxiv.org/abs/2104.05556 (2021).
49. Luo, Y. et al. A unique van Hove singularity in kagome superconductor $CsV_{3-x}Ta_xSb_5$ with enhanced superconductivity. *Nat. Commun.* **14**, 3819 (2023).
50. Feng, X. Y. et al. Commensurate-to-incommensurate transition of charge-density-wave order and a possible quantum critical point in pressurized kagome metal CsV_3Sb_5. *npj Quantum Mater.* **8**, 23 (2023).
51. Sobota, J. A., He, Y. & Shen, Z. X. Angle-resolved photoemission studies of quantum materials. *Rev. Mod. Phys.* **93**, 025006 (2021).
52. Kresse, G. & Furthmüller, J. Efficiency of ab initio total energy calculations for metals and semiconductors using a plane-wave basis set. *Comput. Mater. Sci.* **6**, 15 (1996).
53. Kresse, G. & Furthmüller, J. Efficient iterative schemes for ab initio total-energy calculations using a plane-wave basis set. *Phys. Rev. B* **54**, 11169 (1996).
54. Liu, B. et al. Tunable van Hove singularity without structural instability in kagome metal $CsTi_3Bi_5$. *Phys. Rev. Lett.* **131**, 026701 (2023).

Acknowledgements

We thank T. Wu, Z. Wang, and J. Ying for useful discussions. The work at University of Science and Technology of China (USTC) was supported by the National Natural Science Foundation of China (Nos. 52273309, 12074358, 52261135638, 11974327, 12004369, 11888101), the Fundamental Research Funds for the Central Universities (Nos. WK3510000015, WK3510000012, WK2030000035), the International Partnership Program of the Chinese Academy of Sciences (No. 123GJHZ2022035MI), the Innovation Program for Quantum Science and Technology (Nos. 2021ZD0302802, 2021ZD0302800), the Anhui Initiative in Quantum Information Technologies (No. AHY170000), and the USTC start-up fund. This work was partially carried out at the Instruments Center for Physical Science, University of Science and Technology of China. We also thank the Supercomputing Center of USTC for providing the high-performance computing resources.

Author contributions

L.H., H.L., Y.H., and Y.L. contributed equally to this work. J.H. proposed and designed the research. L.H., Y.L., S.P., Z.W., J.S., B.W., Y.M., X.S., Z.O., B.L., X.Y., and J.H. contributed to the development of the ARPES system and performed the ARPES measurements. H.L., Z.X., and X.C. grew and characterized the samples. Y.H., M.-Q.K., and Z.Q. performed the calculations. L.H. and J.H. wrote the paper with inputs from all authors.

Competing interests

The authors declare no competing interests.

Additional information

Supplementary information The online version contains supplementary material available at https://doi.org/10.1038/s41535-024-00635-5.

Correspondence and requests for materials should be addressed to Zhenhua Qiao, Xianhui Chen or Junfeng He.